

W. SWIDCIR

NRL Memorandum Report 2907

Research at NRL on Theoretical and Numerical Simulation Studies of Ionospheric Irregularities

S. L. OSSAKOW

*Plasma Dynamics Branch
Plasma Physics Division*

October 1974



NAVAL RESEARCH LABORATORY
Washington, D.C.

Approved for public release; distribution unlimited.

ADA002930

UNCLASSIFIED

SECURITY CLASSIFICATION OF THIS PAGE (When Data Entered)

| REPORT DOCUMENTATION PAGE | | READ INSTRUCTIONS BEFORE COMPLETING FORM |
|--|-----------------------|--|
| 1. REPORT NUMBER NRL Memorandum Report 2907 | 2. GOVT ACCESSION NO. | 3. RECIPIENT'S CATALOG NUMBER |
| 4. TITLE (and Subtitle) RESEARCH AT NRL ON THEORETICAL AND NUMERICAL SIMULATION STUDIES OF IONOSPHERIC IRREGULARITIES | | 5. TYPE OF REPORT & PERIOD COVERED An interim report on a continuing problem |
| 7. AUTHOR(s) S. L. Ossakow | | 6. PERFORMING ORG. REPORT NUMBER |
| 9. PERFORMING ORGANIZATION NAME AND ADDRESS Naval Research Laboratory Washington, D.C. 20375 | | 10. PROGRAM ELEMENT, PROJECT, TASK AREA & WORK UNIT NUMBERS DNA S99QAXHC04001 ONR RR033-02-42-5308 NAVAIR WF 52551701 |
| 11. CONTROLLING OFFICE NAME AND ADDRESS Defense Nuclear Agency Washington, D.C. 20305 Office of Naval Research Arlington, Va. 22217 | | 12. REPORT DATE October 1974 |
| 14. MONITORING AGENCY NAME & ADDRESS (if different from Controlling Office) | | 13. NUMBER OF PAGES 36 |
| 16. DISTRIBUTION STATEMENT (of this Report) | | 15. SECURITY CLASS. (of this report) UNCLASSIFIED |
| 17. DISTRIBUTION STATEMENT (of the abstract entered in Block 20, if different from Report) | | 15a. DECLASSIFICATION/DOWNGRADING SCHEDULE |
| 18. SUPPLEMENTARY NOTES | | |
| 19. KEY WORDS (Continue on reverse side if necessary and identify by block number) Ionosphere Scintillations Striations Type II Electrojet Irregularity | | |
| 20. ABSTRACT (Continue on reverse side if necessary and identify by block number) The importance of ionospheric irregularities in the overall concept of dynamic ionospheric physics modeling is emphasized. In particular, ionospheric irregularities produce scintillation which cause communication and radar system degradation. The determination, classification and nonlinear development of such instabilities, in terms of theoretical and numerical studies, is of fundamental importance in giving the Navy and other systems users a predictive capability in combating deleterious scintillation effects. A research (continued) | | |

UNCLASSIFIED

SECURITY CLASSIFICATION OF THIS PAGE(When Data Entered)

20. Abstract (continued)

program in theoretical and numerical simulation of ionospheric irregularities has been set up in the Plasma Dynamics Branch. This report gives an overview of ionospheric irregularities and specific results in two areas: (i) nonlinear development of the type II E region equatorial electrojet instability; and (ii) plasma clouds, image effects and striations in the ionosphere.

UNCLASSIFIED

SECURITY CLASSIFICATION OF THIS PAGE(When Data Entered)

CONTENTS

| | <u>Page</u> |
|---|-------------|
| I. Introduction | 1 |
| II. Importance of Studies | 3 |
| III. Simplified Scintillation Geometry | 5 |
| IV. Particular Examples of Irregularities Studied | 7 |
| A. Equatorial Electrojet-Type II Instability | 8 |
| B. Striations and Cloud Morphology Associated with Plasma Clouds Coupled to the Background Ionosphere | 14 |
| V. Summary | 23 |
| Acknowledgements | 25 |
| References | 26 |

RESEARCH AT NRL ON THEORETICAL AND NUMERICAL
SIMULATION STUDIES OF IONOSPHERIC IRREGULARITIES

I. Introduction

The general problem of ionospheric modeling, important for predictive capabilities in communication and radar systems, can be broken up into three categories: (1) data collection; (2) model development; and (3) systems applications. The Plasma Dynamics Branch, the theoretical and computational arm of the Plasma Physics Division, has been engaged in the second category of dynamic ionospheric modeling for about two years. This research is being carried out under the auspices of ONR, NAVAIR, and DNA. The general modeling categories can be broken up into the following subsections: (i) chemistry; (ii) neutral atmosphere; (iii) laminar ionosphere; and (iv) turbulent or irregular ionosphere. The work which will be reported on in this paper is an overview of the studies carried out in area (iv) which we call ionospheric plasma irregularities. Study of the turbulent ionosphere requires a knowledge of the laminar ionosphere which in turn requires a knowledge of the chemistry and the neutral atmosphere. Thus, for a time predictive capability areas (i) - (iv) must be studied. A program addressing all of these areas is being developed. The present report will, however, address only the problem of ionospheric irregularities.

Initially the work involved the development of the capability to treat, computationally and theoretically, the non-linear dynamics of ionospheric plasmas. The capability, once developed, was then applied to several outstanding problems. Three of the problems are: (A) Type II equatorial electrojet instabilities; (B) Striations in plasma clouds and image formation in plasma cloud-ionosphere coupled systems; and (C) Ionospheric spread F. Radar backscatter¹ observations of three meter

irregularities, i.e., electron density fluctuations, in the geomagnetic equatorial E region electrojet have led us to study process A. Barium clouds^{2,3} released by rockets in the upper ionosphere and high altitude nuclear releases both of which exhibit field aligned striations, i.e., electron and ion density fluctuations, led us to the study of process B. Scintillation of radio signals from polar orbiting⁴ and equatorial satellites^{5,6} and ionosonde data^{7,8,9} have led us to study process C (also due to electron density fluctuations). All three processes can cause scintillation or enhanced backscatter. These three processes are caused by plasma instabilities which depend on the fact that electrons and ions collide with neutral particles. In particular, the instabilities causing the first two processes (A and B) arise from having an electron density gradient and electron and ion-neutral drag effects transverse to the ambient magnetic field. This instability is called the E X B gradient drift instability.^{10,11,12,13,14} Process C, in the case of midlatitude Spread F, is believed to depend upon the fact that as the plasma in a flux tube is moved up or down in altitude it samples regions of different Pedersen conductivity¹⁵. The inadequacy of linear theory to describe these phenomena has led us to study by theoretical and numerical simulation techniques the nonlinear development of these three processes (plasma instabilities).

II. Importance of Studies

The basic importance of our studies on ionospheric irregularities can be catalogued as follows: (1) the instabilities degrade communications; (2) the instabilities degrade radar performance; and (3) the studies will enable us to obtain a predictive capability with respect to (1) and (2), i.e., where to expect these irregular structures and what their properties will be. At this juncture let us elaborate on (1).

The fact that time-varying irregular structure in the ionosphere (known as ionospheric scintillation) could affect radio signals emitted by stars has been known for some time^{16,17}. However, only recently, and then with some surprise, has it been found that the ionosphere can seriously perturb signals used for satellite communications¹⁷. The effect of irregular structure, i.e., irregularities of the refractive index, in the ionosphere is to superpose a random fluctuation of signal amplitude, phase and polarization. These deleterious effects may cause an intolerable number of errors in the received signal and produce unusable information. Utlaut¹⁷ has recently pointed out that (a) some of the orbiting meteorological satellites transmitting video weather data have experienced conditions during which the video data were nearly obscured as a result of scintillation; (b) a navigation satellite system has experienced difficulties inserting ephemeris data in the spacecraft at times because of scintillation; and (c) signals from geostationary satellites may also suffer deleterious effects, in regions other than the equatorial region, when transmitting to higher latitudes

since the polar cap scintillating region is tipped with respect to the geographic pole (e.g., aircraft routes near midlatitude over the North Atlantic could experience difficulties communicating by way of geostationary satellites). Naturally occurring scintillation is strongest in the high latitude (auroral and polar regions) and equatorial regions¹⁷,¹⁸, although midlatitude scintillation also occurs^{19,20,21}. However, these notions refer to natural scintillations. U. S. high altitude nuclear releases (e.g. Starfish) have produced world wide spread F with attendant scintillation phenomena^{22,23,24}. Also, Russian releases at Novaya Zemlya, U.S.S.R. in October 1961 produced E and F region irregularities in the Scandinavian area²⁵.

Although much of the scintillation observations have been restricted to VHF¹⁷, recent results of equatorial scintillation in the 1-6 GHz regime^{5,6,17} show that one cannot merely go to higher frequencies to escape scintillation effects. Much of the scintillation observations come from ground based receivers (mostly in VHF and UHF regime, with a small amount of SHF data) although limited in situ measurements²¹ are also available. These observations have provided valuable information about scintillation phenomena; however, the effects of variation of signal parameters important for system design or systems performance prediction is almost nonexistent. More fundamental is the lack of understanding of the basic physical processes involved in the formation of ionospheric irregularities which cause scintillation. The limited amount of observational data coupled with limited theoretical understanding make it impossible to now predict how communications systems will perform in natural or artificial scintillation environments. For

the high data rate, broadband transmitters now planned for Navy, other DOD and commercial communication satellites it is imperative to understand scintillation phenomena, for severe scintillations over several seconds can mean loss of information (message).

Ionospheric physicists, systems designers, modelers and wave propagationists have noted^{17,26} the need for theoretical studies to determine the underlying mechanisms responsible for ionospheric scintillation so that a true predictive capability can be achieved. The inadequacy of empirical modeling²⁶ of ionospheric scintillation, the recent in situ measurements of ionospheric scintillation²¹, and advances in theoretical and computational plasma physics^{15,27-33} make this a propitious time for further theoretical and numerical studies of scintillation phenomena. The theoretical and computational programs at NRL are at a state, where we can generate detailed information on the causes and structure of ionospheric irregularities. The results of this work can provide a basis for interpretation of experimental data; suggest new experiments; aid in the design of new communication systems and provide a framework within which to improve the performance of existing systems.

III. Simplified Scintillation Geometry

Before proceeding with a description of examples of the work we are doing on ionospheric irregularities, we will give a brief discussion, albeit simple, on what is involved in scintillation phenomena. The interested reader can obtain a more complete understanding of propagation through ionospheric irregularities by consulting the appropriate references^{20,34-41}.

Figure 1 shows a simplified view of what happens in scintillation phenomena. We consider a plane wave (signal) propagating in the z direction where it is emitted by a transmitter (source) and enters a layer where there are irregularities, i.e., density fluctuations (shown by ellipses in the x - y diffracting plane). On emergence from the irregularities layer, properties of the wave front are related to properties of the irregularities. In most cases of interest absorption in the layer is negligible. Also, the irregularity layer can usually be replaced by an equivalent thin screen of negligible thickness. Field fluctuations near the screen are of phase only; however, amplitude scintillations develop as the wave travels away from the screen. For these conditions the relationship between the intensity scintillation spectrum, $P_S(k)$, and the irregularities density fluctuation spectrum, $P_N(k)$ is³⁴

$$P_S(k) = 8\pi L (r_e \lambda)^2 P_N(k) \sin^2(k/k_f)^2 \quad (1)$$

where L is the equivalent layer thickness, r_e is the classical radius of the electron ($r_e = e^2/mc^2$), λ is the radio wavelength of the signal, k is the wavenumber of the irregularity of interest ($k^2 = k_x^2 + k_y^2$), k_f is the Fresnel wavenumber ($k_f^2 = 4\pi/\lambda z$, where z is the mean height of the scattering layer). Equation 1 gives the expected two-dimensional diffraction pattern at the receiving plane. Indeed the integral, $2\pi \int_0^\infty P_S(k) k dk$ is basically the scintillation index S_4 used by ionospheric workers. The important point is that there exists a simple relationship between $P_S(k)$ and the power spectrum $P_N(k)$ of the irregularities (even for thick screens; see reference 20). $P_S(k)$

determines the diffraction pattern and $P_N(k)$ determines $P_S(k)$. Thus what we wish to find out from the theoretical and numerical simulation studies is the power spectrum, $P_N(k)$, of the density fluctuations among other things. To date, $P_N(k)$ is assumed by ionospheric workers (based on at best limited data on scintillation phenomena). To obtain $P_N(k)$ from theoretical and numerical simulation analysis will give a true predictive capability.

IV. Particular Examples of Irregularities Studied

Before proceeding to discuss our work on the type II electrojet instability and striations, as examples, in sections A and B below (work on midlatitude spread F is in the beginning stages), we will briefly outline the methods of solution which are involved and basically common to all three processes A, B, and C mentioned in Section I. The methods involved are (1) large scale numerical simulation of the appropriate system of coupled nonlinear differential equations which are derived theoretically and thought to represent the process being studied; (2) the geometry is basically two-dimensional, i.e., the dimension parallel to the ambient magnetic field, B_0 , is integrated out; (3) there are continuity equations for the density and/or cross field (Pedersen) conductivity of the appropriate electron and ionic species; (4) momentum equations for the appropriate species; and (5) a potential-like equation arising from the fact that the divergence of the current is zero ($\nabla \cdot \underline{J} = 0$).

The two dimensional geometry is a fairly good representation of the processes being studied. Full three dimensional studies would tax the capability of present day computers. The momentum equation in (4) usually reduces to an algebraic equation in which the velocity of the particular species is related to the transverse electric fields (and/or neutral winds) and ambient magnetic field by means of cross field mobilities. Assuming the electric fields derivable from a potential (the electrostatic approximation valid for the ionosphere) results in a potential-like equation when the velocities are inserted into the current condition, $\nabla \cdot \underline{J} = 0$. All these ideas will become clearer in sections A and B below.

A. Equatorial Electrojet - Type II Instability

To serve as a background for this section, Figure 2 shows a model of the daytime electrojet (see references 42 and 43) and how the radar views it. The electrojet is a highly conducting layer usually between 100 and 110 km located at the geomagnetic equator (within $\pm 2^\circ$). The eastward field, \underline{E}_D , results from atmospheric tidal motion and the vertical electric field, \underline{E}_P , is the resulting vertical polarization field which suppresses vertical currents. (This condition gives $E_P = (\sigma_H/\sigma_P) E_D$, where σ_H and σ_P are the Hall and Pedersen conductivities respectively and $\sigma_H/\sigma_P \sim 20-30$). It is this vertical field which drives the electrojet by Hall currents. Since the electron-neutral collision frequency is much less than the electron cyclotron frequency ($\nu_e \ll \Omega_e$) and the ion-neutral collision frequency is much greater than the ion cyclotron frequency ($\nu_i \gg \Omega_i$; ions are essentially at rest with

respect to the neutrals), the resulting electron-ion drift velocity is $v_o \approx \frac{cE_p}{B_o}$ (cgs units will be used throughout) and in the westward direction. This is essentially the electron drift so that the current is in the eastward direction. Also there is a vertical electron density gradient with a scale height $(N_o/dN_o/dz) \sim 6-10$ km. The reason why the electrojet is localized in altitude is that above this region while N_o is increasing the collision frequency is decreasing and so the conductivity is low. However, below this region while the collision frequency is increasing the electron density is decreasing and so again the conductivity is low. The reason why the electrojet is located at the geomagnetic equator is deduced by considering the concept of a stratified ionosphere and the concept of layered conductivity⁴⁴. Basically the requirement that there be no vertical current reduces the 3×3 conductivity tensor to a 2×2 tensor representing a layered conductivity with horizontal flow. Into such an expression comes the dip angle (angle between the magnetic field and the horizontal direction). It can be shown that when the dip angle is zero the cross field conductivity becomes a maximum. Referring to Fig. 2 the radar observes the electrojet by backscatter so that a wave launched with wavevector \underline{k}_R sees a return with $-\underline{k}_R$ and the relation between the radar wavelength and the irregularity wavelength is $2 |\underline{k}_R| = |\underline{k}_I|$ where $k = 2\pi/\lambda$ and λ is the wavelength. (So that the radar wavelength is twice the wavelength of the irregularity that it samples). The radar at Jicamarca, Peru where the observations are made operates in the 15 MHz-150 MHz range (irregularity wavelengths 10 - 1 meter).

There are two types of instabilities, producing density fluctuations, associated with the electrojet configuration shown in Fig. 2. In this paper we will be addressing the type II instability. This is excited when the electron current across B_0 is less than the ion sound speed (i.e., $V_0 <$ ion sound speed). This instability has no velocity threshold and travels at the drift velocity of the electrons. The observed backscatter is generally believed to be due to this gradient drift instability^{13,14,45-47}. However, we will see shortly that linear instability theory doesn't bear this out for the radar wavelengths observed. The basic equations governing the dynamics of the electrojet are^{32,33}

$$\frac{\partial N_e}{\partial t} + \nabla \cdot (N_e \underline{V}_e) = 0 \quad (2)$$

$$\frac{e}{m_e} (\underline{E} + \frac{V_e}{c} \times \underline{B}_0) + \frac{U_e^2}{N_e} \nabla N_e + \nu_e \underline{V}_e = 0 \quad (3)$$

$$\frac{\partial N_i}{\partial t} + \nabla \cdot (N_i \underline{V}_i) = 0 \quad (4)$$

$$\left(\frac{\partial}{\partial t} + \underline{V}_i \cdot \nabla \right) \underline{V}_i = - \frac{U_i^2}{N_i} \nabla N_i + \frac{e}{m_i} \underline{E} - \nu_i \underline{V}_i \quad (5)$$

$$N_e = N_i = N \quad (6)$$

where the subscripts e and i refer to electrons and ions, U_e and ν_e are the electron thermal speed and electron-neutral collision frequency,

respectively, $\underline{E} = -\nabla\phi$ is the electric field (electrostatic assumption), \underline{B}_0 is the earth's magnetic field (assumed constant and in the x direction), N is density and \underline{v} is bulk velocity. The inclusion of the left hand side eqn. (5), i.e., ion inertia, is not really necessary for type II studies. However, it is important for type I studies ($V_o >$ ion sound speed) and we retain it for generality. Equation (3) contains magnetic terms ($\nu_e \ll \Omega_e$) showing the electrons are tied to the field lines, while eqn (5) exhibits no such terms ($\nu_i \gg \Omega_i$) showing the ions to be tied to the neutrals.

A linear stability analysis of eqns. (2)-(6) with perturbations assumed to be of the form $\exp i(k_y y - \omega t)$, where $\omega = \omega_r + i\gamma$ (so that positive γ represents the growth rate), has been performed. For electrojet parameters^{32,33}, $\Omega_e = 5 \times 10^6 \text{ sec}^{-1}$, $\nu_e = 4 \times 10^4 \text{ sec}^{-1}$, $\nu_i = 2.5 \times 10^3 \text{ sec}^{-1}$, $C_s^2 = 10^5 \text{ m}^2/\text{sec}^2$, (where $C_s^2 = U_i^2 + U_e^2 m_e/m_i$) $V_o = 100 \text{ m/sec}$ ($V_o < C_s$, ion sound) and $(N_o/dN_o/dz) = 6 \times 10^3 \text{ m}$, unstable gradient drift waves result in the y direction with a minimum wavelength of ~ 30 meters (see Fig. 3). However, radar backscatter results¹ show unstable waves, i.e., enhanced density fluctuations ~ 3 meters. In order to resolve this dilemma, we have studied the nonlinear evolution of the electrojet equations (2) - (6), in the y-z plane, by numerical simulation³³.

Before proceeding with the numerical simulation, eqns. (2) - (6) are recast using

$$\nabla \cdot \underline{J} = e \nabla \cdot \left[N (v_i - \underline{v}_e) \right] \quad (7)$$

As stated previously eqn (7) results in a Poisson-like equation by

algebraically solving eqn. (3) for \underline{v}_e and using an effective potential,

$$\Phi \equiv \frac{e}{m_e} \phi - U_e^2 \ln N \quad (8)$$

The resulting equation for Φ is

$$\nabla^2 \Phi + \left[\nabla \ln N - \frac{\Omega_e}{\nu_e} \times \nabla \ln N \right] \cdot \nabla \Phi = (\nu_e + \frac{\Omega_e^2}{\nu_e}) \frac{1}{N} \nabla \cdot (N \underline{v}_i) \quad (9)$$

where $\Omega_e = e B_0 / m_e c$.

An initial 4% density perturbation^{32,33} of the form $\delta N/N_0 = 0.03$ $\sin k_y y - 0.01 \sin k_z z$, where $k_y = k_z = 2\pi/72$ meters is put into the system at $t = 0$ (see Fig. 4). We are essentially looking at a slice of the electrojet in the $y-z$ plane which is 75 x 75 meters. We then numerically integrate eqns. (4), (5) and (9) and carry it forward in time (see reference 33 for a more complete discussion of the procedure used) and what results is a quasi-final state of turbulence as depicted in Fig. 5.

The density contours depicted in Fig. 5 is the type of turbulent layer that a signal traversing the E region electrojet would see. The relevant information from such a figure is obtained by performing a Fourier analysis of the $(\delta N/N)^2$ and this power spectrum, i.e. the $P_N(k)$ we spoke about in section III, is shown in Fig. 6. We note that this square of the density fluctuation spectral amplitude follows a power law for the shorter wavelengths which agrees well with rocket observations through the equatorial electrojet^{48,49}. It is of interest to note that Spread F in situ²¹ and ground observed^{20,34} scintillation measurements show similar power law dependence of the spectrum.

Type II electrojet results can be summarized as follows: (1) long wavelength (> 30 meters) horizontally propagating gradient drift instabilities generate short wavelength (~ 3 meters) vertically propagating instabilities; (2) the quasi-final state is a highly turbulent two dimensional state with upward and downward moving irregularities with speeds of the order of the horizontal drift speeds; and (3) the power spectrum for density fluctuations in the short wavelength irregularities goes like $k^{-3.5}$. Result (1) agrees with the high resolution radar backscatter data¹ and our basic theoretical ideas^{32,33}. It basically shows a cascading of energy from longer linearly unstable wavelengths to shorter, linearly stable wavelengths. Result (2) also agrees well with the radar backscatter data¹. Result (3) agrees well with the rocket observations^{48,49} and dimensional arguments⁵⁰.

This is the first numerical simulation ever done of the type II electrojet phenomena and has aided considerably in the understanding of such phenomena. Further simulations are on going to obtain finer resolution for the shorter wavelengths (see Fig. 6 and comments therein) and also increasing V_o so that the intermediate regime between type II and type I can be studied. The capability which has been developed for this problem can also be used to study the stability of the auroral electrojets.

B. Striations and Cloud Morphology Associated With Plasma

Clouds Coupled to the Background Ionosphere

We will now discuss our two-layered model for striation and image cloud development when plasma clouds exist in and are coupled to the background ionosphere. Striations are magnetic field-aligned irregularities such as are seen in barium plasma clouds^{2,3} released in the ionosphere and in the late time development of high altitude nuclear explosions. These phenomena are often diagnosed by optical techniques. If, however, these striations induced irregularities in other regions of the ionosphere such irregularities would be invisible to the naked eye, but not to radar or communication signals that pass through them. Indeed, these image effects, as we shall call them, could have a profound effect on such signals. Although we have spoken of artificially released plasma clouds inducing these image effects, the basic ideas are equally applicable to naturally occurring plasma blobs or irregularities that appear in the ionosphere (here the clouds themselves are only visible to radio signals!). Figure 7 shows a simplified view of our basic two-level system for treating plasma clouds coupled to the background ionosphere. Layer 1 represents the level at which the basic plasma cloud exists and layer 2 is the level at which images will occur (in actuality images will extend continuously below the cloud to some level depending on background ionospheric ion-neutral collision frequencies and ratio of cloud to background ionosphere Pedersen conductivity). Each of the two levels is characterized by its own zeroth order parameters such as ion-neutral collision frequencies, cross magnetic field conductivities,

etc. (see for example references 30 and 31). The two regions are electrostatically coupled because of the high conductivity along the magnetic field lines which couple the two layers. Typically we consider cases where the plasma cloud is in the F region and coupled to the E region, i.e., the cloud is around 200-250 km and would produce images down to around 150 km. Figure 7 gives a pictorial view of the plasma cloud in layer 1 with say a gaussian density dependence and the attendant image clouds induced by it in layer 2. The plus and minus sign in layer 2 refer to enhancement of positive ions and depletion of positive ions from the ambient values, respectively. The geometry of the applied electric, \underline{E}_0 , and magnetic, \underline{B}_0 , fields are shown. Perturbations (striations) produced in the plasma cloud will also be exhibited in the image clouds^{30,31}. In the model presented in Fig. 7, ion flow is allowed in each layer and essentially only electron flow between layers (direction depending on direction of \underline{E}_0). The major importance is the coupling of the plasma cloud to other regions of the ionosphere (imaging). Indeed, in certain cases, one can get coupling to the conjugate ionosphere.

The basic starting point of our nonlinear studies of striation phenomena is essentially the set of eqns. (2) - (6). These equations neglect neutral wind effects and we will do so here, initially. It is generally agreed upon that striations in plasma clouds are caused by the $\underline{E}_0 \times \underline{B}_0$ gradient drift instability^{11,12,27} and so the left hand side of eqn. (5) can be neglected. However, because we will be dealing with altitude regimes where ν_i , the ion-neutral collision frequency, is not much greater than Ω_i , the ion cyclotron frequency, a magnetic $\underline{V} \times \underline{B}$ force

term must be included in eqn. (5) which is of the same form as that which appears in eqn. (3). For example the perpendicular ion velocity can then be solved for algebraically in terms of \underline{E} and \underline{B} from eqn (5) and we obtain

$$\begin{aligned} \underline{v}_{\perp i} &= \frac{c}{B_0} \frac{\kappa_i}{1+\kappa_i^2} \left[\underline{E} - \frac{m_i U_i^2}{e} \frac{\nabla N_i}{N_i} \right] \\ &+ \frac{c}{B_0^2} \frac{\kappa_i^2}{1+\kappa_i^2} \left[\underline{E} - \frac{m_i U_i^2}{e} \frac{\nabla N_i}{N_i} \right] \times \underline{B}_0 \end{aligned} \quad (10)$$

where $\kappa_i \equiv \Omega_i / \nu_i$, Ω_i is the ion cyclotron frequency, ν_i is the ion-neutral collision frequency, and \perp denotes perpendicular to the magnetic field (which in this study is in the z direction). The multiplicative factor involving κ_i in eqn. (10) will change depending on what altitude we are considering, i.e., it will be different for layers 1 and 2. In this study we point out that there are basically two sets of ion equations one for the plasma cloud (which we refer to as barium) and one for the background ionospheric ions in layer 2 (see reference 30 for more details). The quasi-neutrality condition eqn (6) becomes

$$N_e = N_i + N_b \quad (11)$$

where i refers to background ionospheric ion and b to barium cloud ion. We take the electric field in eqn. (10) to be $\underline{E} = \underline{E}_0 - \nabla \phi$, where \underline{E}_0 is ambient field. For this section we use the effective potential in the form

$$\Psi = \phi - \frac{m_e U_e^2}{e} \ln N_e \quad (12)$$

and is constant along field lines. We use the continuity eqn (4) for barium ions and integrate over the entire thickness of the barium cloud along the magnetic field line and obtain

$$\begin{aligned}
 \frac{\partial N_b}{\partial t} - \frac{c \nabla \Psi \times \underline{B}_0}{B_0^2} \cdot \nabla N_b = - \frac{(\underline{E}_0 - \nabla \Psi)}{e} \cdot \nabla \sum_p^b \\
 + \frac{\sum_p^b}{e} \nabla^2 \Psi + \frac{2kT}{e} \nabla^2 \sum_p^b
 \end{aligned} \tag{13}$$

where we are in a frame moving with $c \underline{E}_0 \times \underline{B}_0 / B_0^2$, have set $m_e U_e^2 = kT$, have kept terms to first order in $\mu_b / \Omega_b = \kappa_b^{-1}$ where κ_b refers to barium quantities (this is possible because for our F region cloud $\kappa_b \gg 1$), N_b is now only a function of x, y as is \sum_p^b which is

$$\sum_p^b = \frac{ec}{B_0} N_b \frac{\nu_b}{\Omega_b} \tag{14}$$

the height-integrated (field line integrated) Pedersen conductivity of the barium cloud (ν_b / Ω_b is considered to be constant in layer 1). Taking the limit $\kappa_e \rightarrow \infty$ we obtain for the background ionosphere ions

$$\frac{\partial N_i}{\partial t} - \frac{c \nabla \Psi \times \underline{B}_0}{B_0^2} \cdot \nabla N_i = - \text{RHS eqn. (13)} \tag{15}$$

Equation (7) yields after integration over the z direction

$$\begin{aligned}
 - \left(\sum_p^i + \sum_p^b \right) \nabla^2 \Psi + \left(\underline{E}_0 - \nabla \Psi \right) \cdot \nabla \left(\sum_p^i + \sum_p^b \right) \\
 - \frac{\nu_i}{\Omega_i} \left(\underline{E}_0 - \nabla \Psi \right) \times \hat{z} \cdot \nabla \sum_p^i - \frac{2kT}{e} \nabla^2 \left(\sum_p^i + \sum_p^b \right) = 0
 \end{aligned} \tag{16}$$

where the superscript i on \sum refers to the height integrated conductivity for the background ionosphere ions and have used the fact

the Hall conductivity of the ionospheric ions

$$\sum_H \frac{i}{B_0} = - \frac{ecN_i}{B_0} \frac{(\nu_i/\Omega_i)^2}{1 + \left(\frac{\nu_i}{\Omega_i}\right)^2} = - \frac{\nu_i}{\Omega_i} \sum_p \frac{i}{p} \quad (17)$$

(note: ν_i/Ω_i is assumed constant in layer 2; also for a more complete description of the derivation see reference 30). The set of equations (13), (15) and (16) describe the two-level system depicted in Fig. 7 and are two dimensional equations (x, y plane).

The general set of equations describing the two level system are not exactly transparent. Consequently, in order to gain a better understanding of the physics involved in the coupled cloud-ionosphere system, we have broken up our studies into small and large clouds. Here the word small or large is in the electrical sense, i.e., whether the ratio of height-integrated Pedersen conductivity of the cloud to that of the background ionosphere is small or large. The small cloud approximation $\left(\sum_p \frac{i}{p} \sim \epsilon \right)$ results in a great simplification (see reference 30 for a more complete description) of eqns. (13), (15) and (16), albeit still not amenable to analytic solution. In particular, eqn. (16) reduces to a Laplacian operator acting on Ψ with source terms on the right hand side which involve the background ionospheric perturbed Pedersen conductivity. This type of potential equation is much easier to solve, numerically, than eqn. (16). Essentially, the barium cloud motion and ionospheric image motion evolve on a time scale $L B_0 / (c E_0 \epsilon^{1/2})$, where L is the linear dimension of the cloud perpendicular to the magnetic field.

Figures 8 and 9 show the results of such calculations. At $t = 0$, a barium cloud of the form $\sum_p^b \alpha \exp - [x^2 + y^2]/L^2$ is used and then the small cloud forms of eqns (13), (15) and (16) are carried forward in time. The barium cloud drives images of order $\epsilon^{\frac{1}{2}}$ relative to the undisturbed ionosphere (see Fig. 8). At long times the relatively high barium cloud ion density contours (equivalent to Pedersen contours since ν/Ω is assumed constant in each layer), in the limit of zero diffusion, $T \rightarrow 0$, form thin sheets making a definite angle, $\theta = \tan^{-1}(\nu_i/\Omega_i)$, with the $E_0 \times B_0$ cloud velocity. This angular dependence is derived from a basic understanding of the Lagrangian velocity involved in the continuity eqn of the small cloud and the computer simulations bear out this dependence. Figure 9 shows the rotational dependence, in the plane perpendicular to B_0 , on ν_i/Ω_i . The study of small clouds has given us great insight into understanding large cloud phenomenology. Figures 8 and 9 show barium cloud morphology, i.e., the dynamical equilibrium motion (there are no perturbations put into the cloud) which depends on background ionospheric parameters, in the small cloud case, and image cloud formation. Our work on small clouds is continuing in an effort to gain even more understanding. For example, we are now including an altitude dependent neutral wind into the problem and seeing the effects of size and direction of such winds on barium cloud and image cloud morphology.

Our large cloud studies ($\sum_p^b / \sum_p^i \sim 1$) use the full set of eqns. (13), (15), and (16) and the results are more readily interpretable in light of our small cloud studies (see reference 31 for a more complete description). The same gaussian form at $t = 0$ is used for the

large barium cloud. Figure 10 depicts large cloud morphology as a function of conductivity ratio (\sum_p^b / \sum_p^i) for fixed v_b/Ω_b and v_i/Ω_i . The case $\sum_p^b / \sum_p^i = 0.1$ resembles the results from the small cloud equations. We see that as \sum_p^b / \sum_p^i is increased the cloud rotates more into the $E_0 \times B_0$ direction. Indeed as this ratio gets larger more imaging is produced, but the reaction of the images back on the motion of the barium cloud is reduced. The results in the last row of Fig. 10 are for an uncoupled cloud, i.e., it is following a barium cloud without background ionosphere coupling. The $\sum_p^b / \sum_p^i = 4$ case for the barium cloud contours more resembles the uncoupled cloud case. In all cases we see cloud elongation in the $E_0 \times B_0$ direction and backside (side anti-parallel to $E_0 \times B_0$) steepening. Other studies show, in agreement with small cloud results, that as v_i/Ω_i is reduced (to 0.1) the clouds rotate even more into the $E_0 \times B_0$ direction with an attendant reduction in strength of the image cloud.

We have put an initial sinusoidal perturbation of about five wavelengths in the y direction on top of the gaussian clouds depicted in rows 2 and 3 of Fig. 10 to investigate striation growth (see reference 31). However, in terms of striation development a one dimensional cloud is much more illuminating and we present the time development of such a system in Fig. 11. The initial ($t = 0$) density Pedersen conductivity is given as

$$\sum_p^b \propto e^{-x^2/L^2} \left[1 + e^{-3} \sin \frac{10\pi y}{64} \right] + 0.01 \quad (18)$$

where L^2 is 64 and so the zeroth order cloud is gaussian in the x

direction and infinite in the y direction (the term 0.01 represents a constant ionospheric background at the cloud level) and on top of this is the initial perturbation $e^{-3} \sin(10\pi y/64)$, i.e., five wavelengths across the system. In the first row of Fig.11 we see the early time development of cloud, background ionosphere and induced potential. As time progresses we see the backside steepening and backside growth of striations and finger-like formation in the barium cloud which is in agreement with experimental observations^{2,3}. What is of interest is the growth of image striations in the background ionosphere. This has never been reported experimentally as observers have not "looked" for it. Also eqns (13), (15) and (16) in the 1D approximation given by (18) are amenable to a linear stability analysis with a resultant algebraic dispersion relation, something that cannot be performed for the 2D cloud. Figure 12 shows the agreement between the solution of such a dispersion relation yielding the growth rate and the actual numerical simulation depicted in Fig. 11. The breaking of the dots (simulation) from the straight line (theoretical growth) indicates the onset of the nonlinear regime.

We are continuing our studies on large clouds for both 1D and 2D barium clouds. We have gained a great deal of insight into cloud morphology and image formation by studying its dependence on $\sum_p b^i / \sum_p i^i$ and are currently looking at the dependence on v_b / Ω_b and v_i / Ω_i . We still have to determine onset times and scale sizes for striation formation. Just as our small cloud model helped us to understand large clouds, we expect 1D studies to help us understand the more realistic 2D clouds. Indeed, the 1D cloud may be more amenable to discovering the quasi-

final saturation or pinching stage. We also have to look at neutral wind effects in large clouds (as we are doing in small clouds). We have to include E region recombination (i.e., chemistry) and its effects on image formation.

Most researchers have focused on the behavior of the barium cloud itself. However, the major result of our two-layered model results is the importance of image clouds, i.e., coupling of the cloud to the ionosphere, under a host of ionospheric conditions. Indeed images themselves can produce anomalous communication and radar results even if our understanding of the main cloud is complete. Signals may have to go through several regions of turbulence as depicted in Figs. 8, 10, and 11 under the caption cloud and background ionosphere, and the regions over which such perturbations occur can be vast. We have found that images always seem to be produced (to be sure their degree depends on certain parameters). Although the basic development of barium cloud motion and striation formation in these clouds from our large cloud results grossly agrees with experiment^{2,3} (as does limited experiments on small cloud agree with our small cloud results⁵¹), no data is available on image formation. The results of our work on coupled plasma cloud-ionosphere phenomena has encouraged SRI to look for image effects in a forthcoming series of barium cloud releases at auroral latitudes. We look forward with great anticipation to these experiments.

V. Summary

We have presented in Section IV A and B two classes of problems under the topic of ionospheric irregularities. Our work on midlatitude nonlinear spread F is proceeding and preliminary results indicate a power law for the power spectrum which is in agreement with the recent in situ measurements²¹. We wish to reiterate that the theoretical and computational programs are at a stage where we can generate detailed information on the causes and structure of ionospheric irregularities, as manifested in sections IV A and B. Essentially as a result of our expertise and experience gained in the high altitude nuclear problem we have been able to make significant contributions on a time scale of about one year. The problems remaining to be done can be accomplished over a reasonable time period, i.e., we are applying existing technologies to gain a basic understanding of the causes and formation of ionospheric irregularities. The results we obtain provide a basis within which to interpret experimental data, suggest new experiments, and acts as a vehicle for suggesting systems design. Understanding the results in terms of the physical processes involved leads to a true predictive capability, i.e., we can know what, when and where to expect irregularities. We can use our theoretical and computational modeling in areas where data is sparse or non-existent, after of course it has proven valid in areas where data exists. In the end, this predictive capability is very much needed for useful systems design.

The major emphasis of this report has been on particular types of ionospheric irregularities. However, in this concluding section, we would like to enumerate our recent accomplishments in ionospheric model development and list future possibilities (specific future areas of study in ionospheric irregularities have been given in sections IV A and B). The accomplishments are: (1) development of midlatitude 1D ionosphere model⁵²; (2) study of the role of resonantly scattered radiation in maintaining the nighttime E region⁵³; (3) study of the response of the F region to EUV flares; (4) proper treatment of the role of oxygen recombination in the tropical nightglow⁵⁴; (5) explanation of the non-thermal features of the auroral plasma due to precipitating electrons^{55,56}; (6) development of an ionospheric model for currents, electric field, and plasma density in an auroral arc⁵⁷; (7) development of the numerical capability to treat the coupling between ion clouds and the background ionosphere, including imaging effects^{30,31}; (8) determination of the nonlinear state of plasma turbulence for type II equatorial electrojet irregularities³³; (9) determination of the importance of parallel propagation effects on the type I electrojet instability⁵⁸; and (10) development of a theoretical model which suggests the presence of intense ion heating in the topside ionosphere due to electrostatic ion cyclotron turbulence⁵⁹.

Future possibilities are: (1) predictive two and three dimensional global ionospheric models; (2) predictive two and three dimensional global, dynamic models of the upper neutral atmosphere; (3) three dimensional models of the wind systems in the polar ionosphere; (4) theoretical and numerical models of the ionosphere-magnetosphere

coupling phenomena; (5) models of the ionospheric effects of substorms and magnetic storms; (6) determination, classification and effects of the most important instabilities which cause ionospheric scintillation; and (7) generation of libraries of model ionospheres for propagation studies (systems users).

We look back to our results with a feeling of accomplishment and to our future studies with a sense of excitement and anticipated accomplishment.

ACKNOWLEDGEMENTS

The work reported herein could only have been completed with the cooperation of my colleagues. As such, I am deeply indebted to David Book, Timothy Coffey, Bob Goldman, Ed McDonald and Tony Scannapieco whose interest and work in ionospheric irregularities is the sine qua non without which this report could not have been written.

REFERENCES

1. B. B. Balsley, and D. T. Farley, "Radar Observations of Two-Dimensional Turbulence in the Equatorial Electrojet," J. Geophys. Res., 78, 7471, 1973.
2. N. W. Rosenberg, "Observations of Striation Formation in a Barium Ion Cloud," J. Geophys. Res., 76, 6356, 1971.
3. T. N. Davis, G. J. Romick, E. M. Wescott, R. A. Jeffries, D. M. Kerr, and H. M. Peek, "Observations of the Development of Striations in Large Barium Ion Clouds," Planet. Space Sci., 22, 67, 1974.
4. E. Nielsen, and J. Aarons, "Satellite Scintillation Observations over the Northern High Latitude Regions," J. Atmos. Terr. Phys., 36, 159, 1974.
5. H. D. Craft, Jr., and L. H. Westerlund, "Scintillations at 4 and 6 GHz Caused by the Ionosphere," AIAA Pap. 72-179, Amer. Inst. of Aeronaut. and Astronaut. Libr., New York, 1972.
6. R. R. Taur, "Ionospheric Scintillation at 4 and 6 GHz," Comsat Tech. Rev., 2, 145, 1973.
7. D. T. Farley, B. B. Balsley, R. F. Woodman, and J. P. McClure, "Equatorial Spread F: Implications of VHF Radar Observations," J. Geophys. Res., 75, 7199, 1970.
8. H. G. Booker, and H. W. Wells, "Scattering of Radio Waves by the F-Region of the Ionosphere," Terres. Magn., 43, 249, 1938.
9. M. L. V. Pitteway, and R. Cohen, "A Waveguide Interpretation of 'Temperate-Latitude Spread F' on Equatorial Ionograms," J. Geophys. Res., 66, 3141, 1961.
10. A. Simon, "Instability of a Partially Ionized Plasma in Crossed Electric and Magnetic Fields," Phys. Fluids, 6, 382, 1963.
11. L. M. Linson, and J. B. Workman, "Formation of Striations in Ionospheric Plasma Clouds," J. Geophys. Res., 75, 3211, 1970.
12. A. Simon, "Growth and Stability of Artificial Ion Clouds in the Ionosphere," J. Geophys. Res., 75, 6287, 1970.
13. K. Maeda, T. Tsuda, and H. Maeda, "Theoretical Interpretation of the Equatorial Sporadic E Layers," Rep. Ionos. Res. Space Res. Jap., 17, 3, 1963.
14. F. B. Knox, "A Contribution to the Theory of the Production of Field-Aligned Ionization Irregularities in the Equatorial Electrojet," J. Atmos. Terr. Phys., 26, 239, 1964.

15. F. Perkins, "Spread F and Ionospheric Currents," J. Geophys. Res., 78, 218, 1973.
16. A. Hewish, "The Diffraction of Galactic Radio Waves as a Method of Investigating the Irregular Structure of the Ionosphere," Proc. Roy. Soc., A214, 494, 1952.
17. W. F. Utlaut, "Ionospheric Scintillations: A Potential Limitation to Satellite Communications - Important Unknown Scintillation Factors," AIAA Pap. 74-56, AIAA 12th Aerospace Sciences Meeting, Jan 30 - Feb. 1, 1974, Washington, D.C.
18. R. U. F. Hopkins, and M. R. Paulson, "Equatorial Scintillation," Naval Research Reviews pg. 17, May-June 1974.
19. J. Aaron, H. E. Whitney, and R. S. Allen, "Global Morphology of Ionospheric Scintillation, " Proc. IEEE, 5, 159, 1971.
20. C. L. Rufenach, "Power-Law Wavenumber Spectrum Deduced from Ionospheric Scintillation Observations," J. Geophys. Res., 77, 4761, 1972.
21. P. L. Dyson, J. P. McClure, and W. B. Hanson, "In Situ Measurements of the Spectral Characteristics of F Region Ionospheric Irregularities," J. Geophys. Res., 79, 1497, 1974.
22. P. Newman, B. Jones, and L. McCabe, "F-Region Irregularities After High Altitude Detonation of July 9, 1962" in Spread-F and its Effects Upon Radiowave Propagation and Communications, P. Newman ed., AGARDOGRAPH 95, Technivision, Maidenhead, England, 1966.
23. H. Maeda, A. J. Shirgaokar, M. Yasuhara, and S. Matsushita, "On the Geomagnetic Effect of the Starfish High-Altitude Nuclear Explosion," J. Geophys. Res., 69, 917, 1964.
24. L. H. Heisler, and L. D. Wilson, "Spread F Development Associated with a High Altitude Nuclear Explosion," Nature, 196, 258, 1962.
25. W. Stoffregen, "Travelling Ionospheric Disturbances Initiated by Low Altitude Nuclear Explosions," Paper 1972/73:14 presented at Specialist Meeting of Electromagnetic Wave Propagation, Wiesbaden, West Germany, 17-21 April 1972.
26. E. J. Fremouw, "Modeling and Prediction of Ionospheric Scintillation," AIAA Pap. 74-54, AIAA 12th Aerospace Sciences Meeting, Jan 30-Feb. 1, 1974, Washington, D.C.
27. H. J. Völkl, and G. Haerendel, "Striations in Ionospheric Ion Clouds, 1," J. Geophys. Res., 76, 4541, 1971.

28. N. J. Zabusky, J. H. Doles III, and F. W. Perkins, "Deformation and Striation of Plasma Clouds in the Ionosphere, 2, Numerical Simulation of a Nonlinear Two-Dimensional Model," J. Geophys. Res., 78, 711, 1973.
29. K. H. Lloyd, and G. Haerendel, "Numerical Modeling of the Drift and Deformation of Ionospheric Plasma Clouds and of their Interaction with other Layers of the Ionosphere," J. Geophys. Res., 78, 7389, 1973.
30. S. R. Goldman, S. L. Ossakow, and D. L. Book, "On the Nonlinear Motion of a Small Barium Cloud in the Ionosphere," J. Geophys. Res., 79, 1471, 1974.
31. A. J. Scannapieco, S. L. Ossakow, D. L. Book, B. E. McDonald, and S. R. Goldman, "Conductivity Ratio Effects on the Drift and Deformation of F Region Barium Clouds Coupled to the E Region Ionosphere," J. Geophys. Res., 79, 2913, 1974.
32. R. N. Sudan, J. Akinrimisi, and D. T. Farley, "Generation of Small-Scale Irregularities in the Equatorial Electrojet," J. Geophys. Res., 78, 240, 1973.
33. B. E. McDonald, T. P. Coffey, S. Ossakow, and R. N. Sudan, "Preliminary Report of Numerical Simulation of Type 2 Irregularities in the Equatorial Electrojet," J. Geophys. Res., 79, 2551, 1974.
34. C. L. Rufenach, "Wavelength Dependence of Radio Scintillation: Ionosphere and Interplanetary Irregularities," J. Geophys. Res., 79, 1562, 1974.
35. S. A. Bowhill, "Statistics of a Radio Wave Diffracted by a Random Ionosphere," J. Res. Nat. Bur. Stand., Sect. D., 65D, 275, 1961.
36. B. H. Briggs, and I. A. Parkin, "On the Variation of Radio Star and Satellite Scintillations with Zenith Angle," J. Atmos. Terr. Phys., 25, 339, 1963.
37. K. G. Budden, "The Amplitude Fluctuations of the Radio Wave Scattered from a Thick Ionospheric Layer with Weak Irregularities," J. Atmos. Terr. Phys., 27, 155, 1965.
38. W. M. Cronyn, "The Analysis of Radio Scattering and Space-Probe Observations of Small-Scale Structure in the Interplanetary Medium," Astrophys. J., 161, 755, 1970.
39. R. V. E. Lovelace, E. E. Salpeter, L. E. Sharp, and D. E. Harris, "Analysis of Observations of Interplanetary Scintillations," Astrophys. J., 159, 1047, 1970.

40. E. E. Salpeter, "Interplanetary Scintillations I. Theory," Astrophys. J., 147, 433, 1967.
41. V. I. Tatarski, Wave Propagation in a Turbulent Medium, McGraw-Hill, New York, 1961.
42. M. Sugiura, and J. C. Cain, "A Model Equatorial Electrojet," J. Geophys. Res., 71, 1869, 1966.
43. M. Sugiura, and D. J. Poros, "An Improved Model Equatorial Electrojet with a Meridional Current System," J. Geophys. Res., 74, 4025, 1969.
44. W. G. Baker, and D. F. Martyn, "Electric Currents in the Ionosphere, I. The Conductivity," Phil. Trans. Roy. Soc. (London), A246, 36, 1953.
45. G. C. Reid, "The Formation of Small-Scale Irregularities in the Ionosphere," J. Geophys. Res., 73, 1627, 1968.
46. A. Register, and N. D'Angelo, "Type 2 Irregularities in the Equatorial Electrojet," J. Geophys. Res., 75, 3879, 1970.
47. J. D. Whitehead, "The Equatorial Electrojet and the Gradient Instability," J. Geophys. Res., 76, 3116, 1971.
48. S. Prakash, S. P. Gupta, and B. H. Subbaraya, "Irregularities in the Equatorial E Region over Thumba," Radio Sci., 4, 791, 1969.
49. S. Prakash, S. P. Gupta, and B. H. Subbaraya, "A Study of the Irregularities in the Night Time Equatorial E-Region Using a Langmuir Probe and Plasma Noise Probe," Planet. Space Sci., 18, 1307, 1970.
50. E. Ott, and D. T. Farley, "The k-Spectrum of Ionospheric Irregularities," J. Geophys. Res., 79, 2469, 1974.
51. G. Haerendel, and R. Lüst, "Electric Fields in the Upper Atmosphere," in Earth's Particles and Fields, edited by B. M. McCormac, Van Nostrand Reinhold, New York, 1968.
52. E.S. Oran, T.R. Young, D.V. Anderson, T. P. Coffey, P.C. Kepple, A.W. Ali, and D.F. Strobel, "A Numerical Model of the Mid-Latitude Ionosphere," NRL Memo Report 2839, July 1974.
53. D. F. Strobel, T. R. Young, R. R. Meier, T. P. Coffey, and A. W. Ali, "The Nighttime Ionosphere E-Region and Lower F-Region," J. Geophys. Res., 79, 3171, 1974.

54. P. S. Julienne, J. Davis and E. Oran, "Oxygen Recombination in the Tropical Nightglow," J. Geophys. Res., 79, 2540, 1974.
55. K. Papadopoulos, and T. Coffey, "Nonthermal Features of the Auroral Plasma Due to Precipitating Electrons," J. Geophys. Res., 79, 674, 1974.
56. K. Papadopoulos, and T. Coffey, "Anomalous Resistivity in the Auroral Plasma," J. Geophys. Res., 79, 1558, 1974.
57. J. A. Fedder, "An Ionospheric Model for Currents, the Electric Field, and the Plasma Density in an Auroral Arc," NRL Memo Report 2691, Jan. 1974; also J. Geophys. Res. to be published.
58. S. L. Ossakow, K. Papadopoulos, J. Orens, and T. Coffey, "Parallel Propagation Effects on the Type I Electrojet Instability," NRL Memo Report 2750, March 1974, also J. Geophys. Res., to be published.
59. P. J. Palmadesso, T. P. Coffey, S. L. Ossakow, and K. Papadopoulos, "Topside Ionosphere Ion Heating Due to Electrostatic Ion Cyclotron Turbulence," Geophys. Res. Letts., 1, 105, 1974.

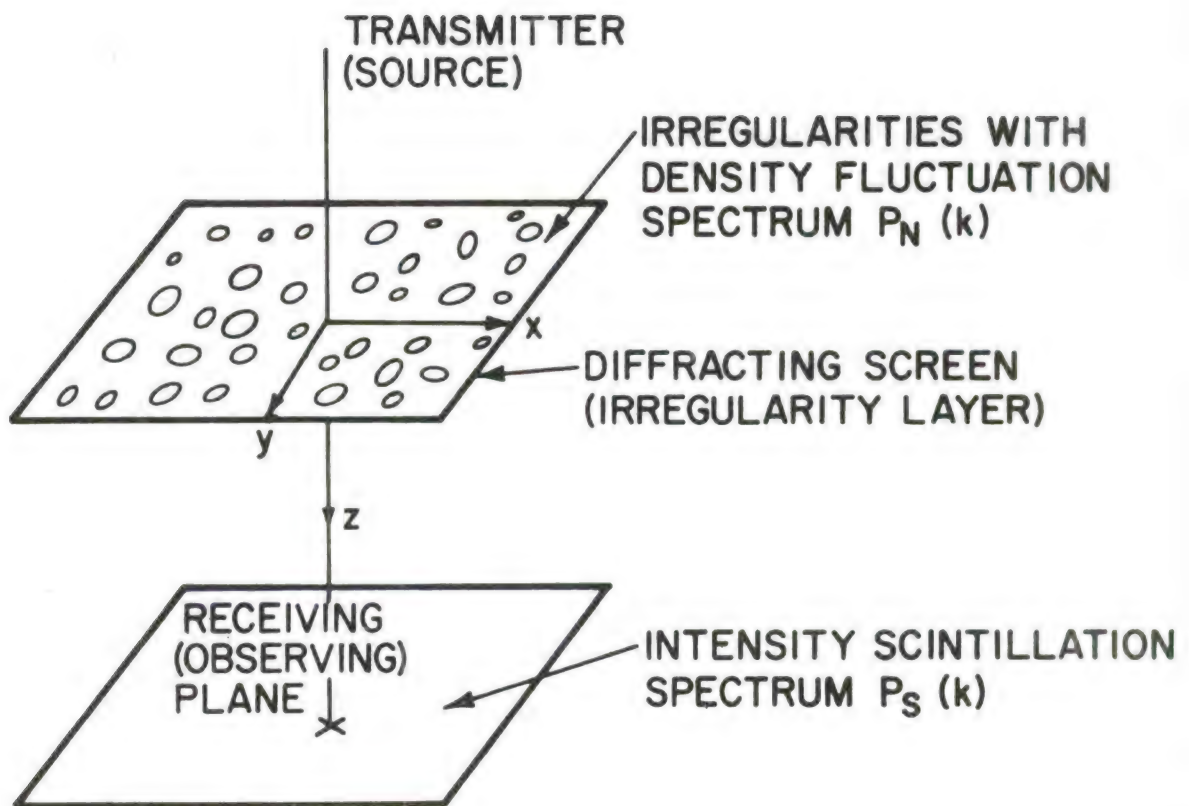


Fig. 1 — Simplified scintillation geometry. A signal traveling in the z direction is incident on a layer of ionospheric irregularities (represented by ellipses). The scintillation power spectrum in the observing plane is related to the power spectrum of the irregularities in the irregularity layer.

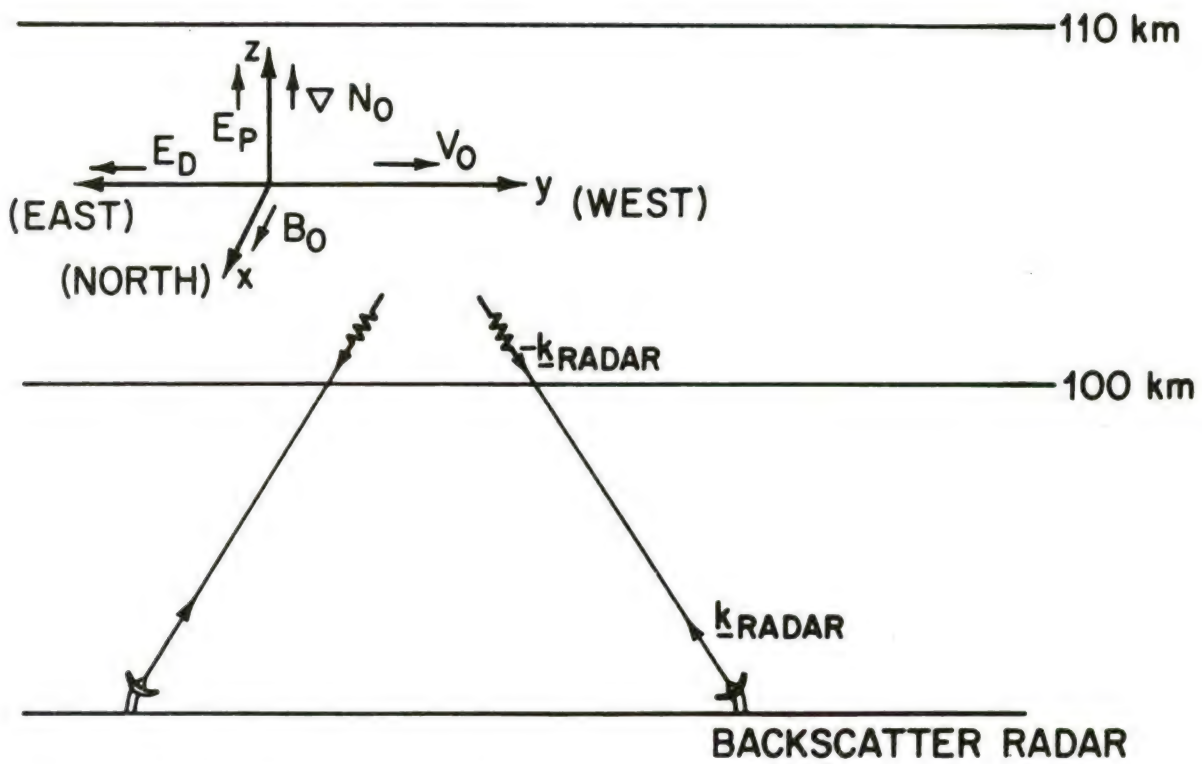


Fig. 2 — Model of daytime equatorial electrojet geometry and observing backscatter radar. The atmospheric tidal electric field E_D , creates a vertical polarization electric field, E_P , which drives the relative electron-ion drift velocity, V_0 , by the Hall effect. This creates an eastward electrojet current. This region of high conductivity is located in the E region ionosphere usually between 100 and 110 km. The earth's ambient magnetic field is taken constant and in the x direction. The vertical equilibrium density gradient, ∇N_0 , has a scale length $\sim 6-10$ km. The radar observes such an electrojet by pure backscatter where the radar wavelength is twice the wavelength of the irregularity it views. The radar at Jicamarca, Peru observes irregularities whose wavelengths are in the 1-10 meter regime.

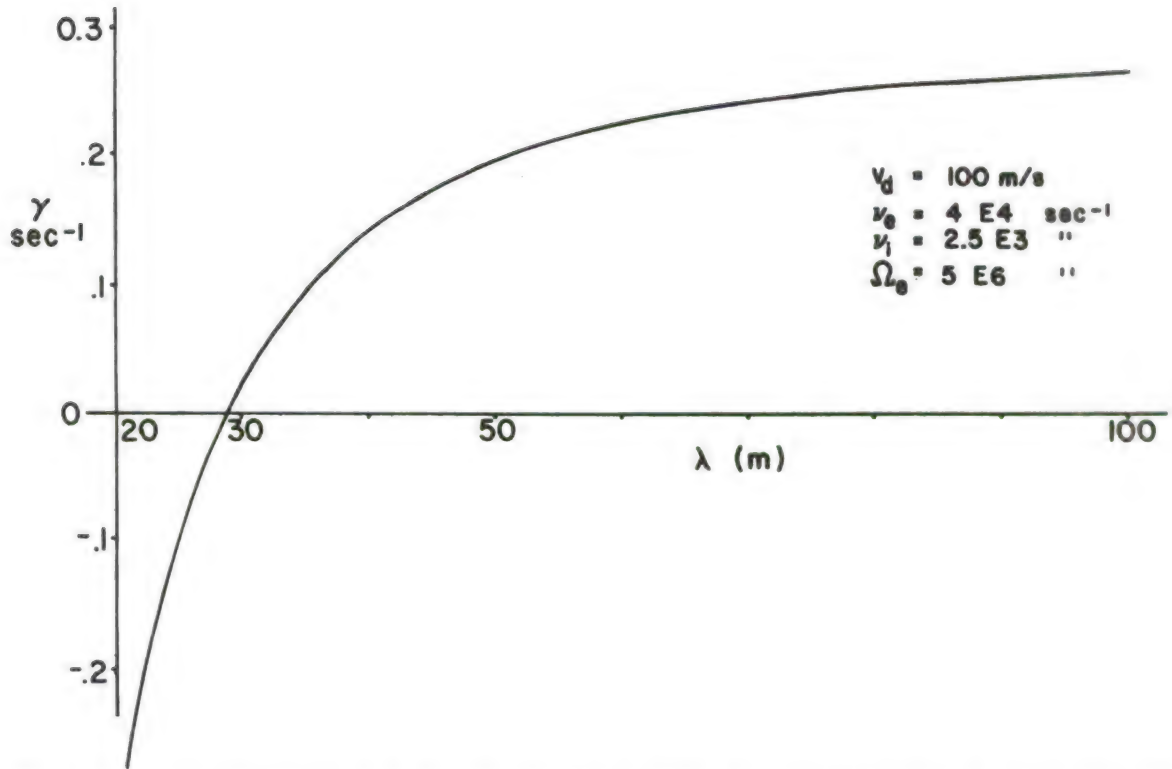


Fig. 3 — Linear stability analysis of Eqs. (2)-(6) which describe the equatorial electrojet, γ vs wavelength. Positive γ indicates growth. For electrojet parameters, $V_o = 100 \text{ m/sec}$, $\nu_e = 4 \times 10^4 \text{ sec}^{-1}$, $\nu_i = 2.5 \times 10^3 \text{ sec}^{-1}$ and $\Omega_e = 5 \times 10^6 \text{ sec}^{-1}$ only waves greater than 28 meters are unstable.

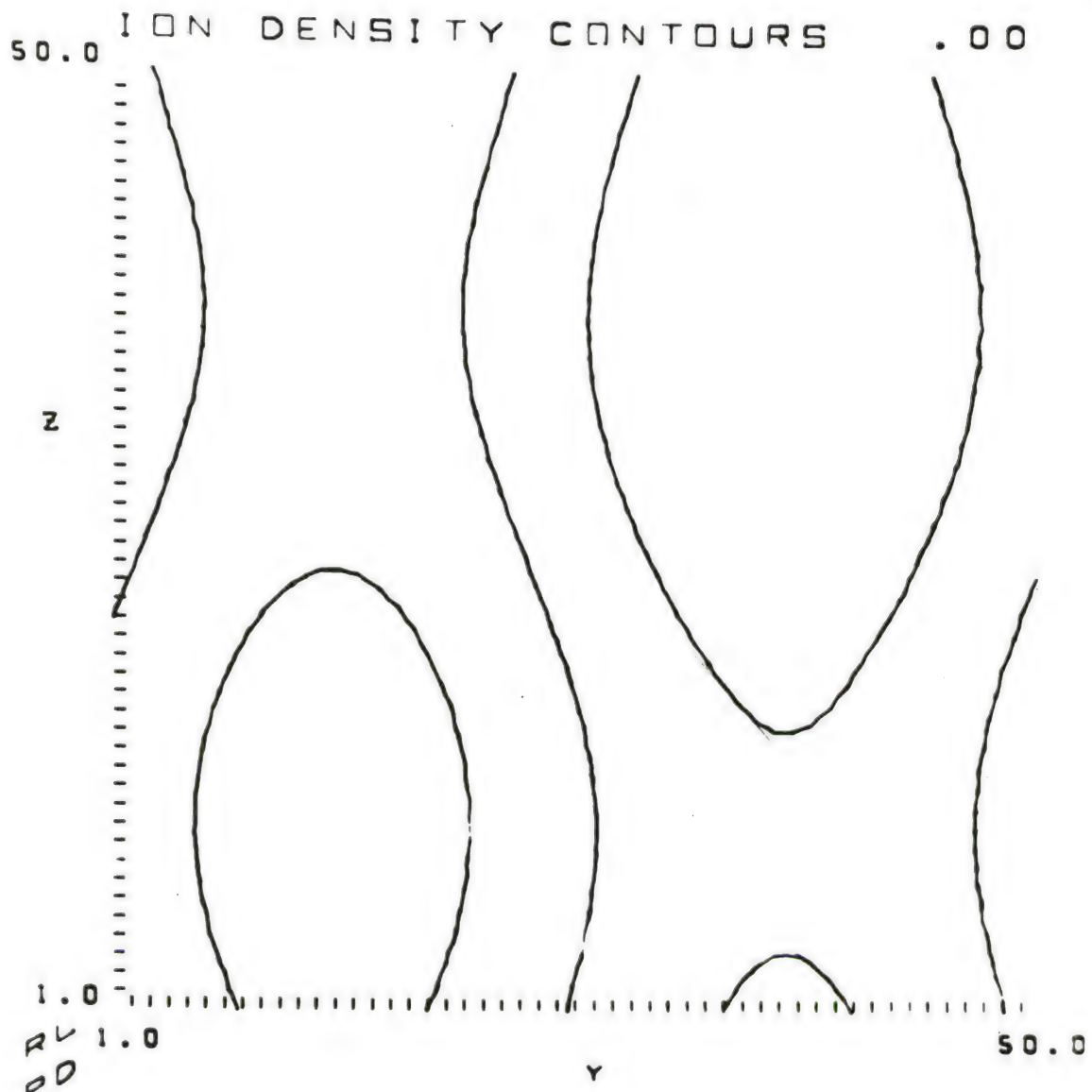


Fig. 4 — Initial electrojet type II perturbation at $t = 0$ used in numerical simulation. These are the iso-density contours. The grid used in producing these results was 50×50 mesh points denoted by tick marks with a 1.5 meter mesh spacing in both directions (y, z), which models the electrojet geometry in Fig. 2. Periodic boundary conditions were employed.

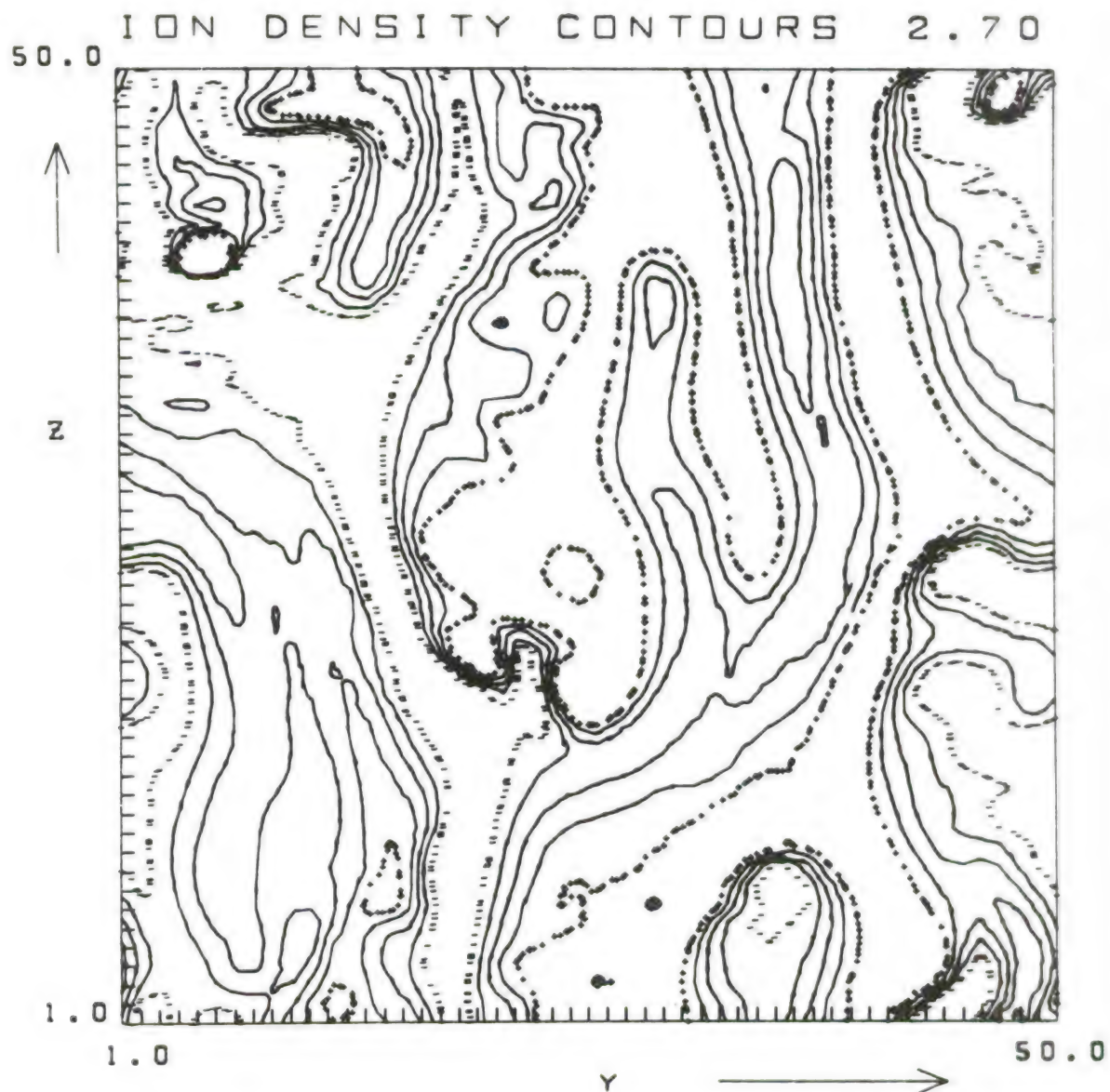


Fig. 5 — Density contours of type II electrojet at $t = 2.7$ sec. The contours in Fig. 4 have evolved to this two dimensional turbulent state via the electrojet Eqs. (2)-(6). The contour spacing is 2.5% of ambient density and the plus and minus signs represent 105 and 95%, respectively. This is the type of irregular structure that propagating signals would pass through.

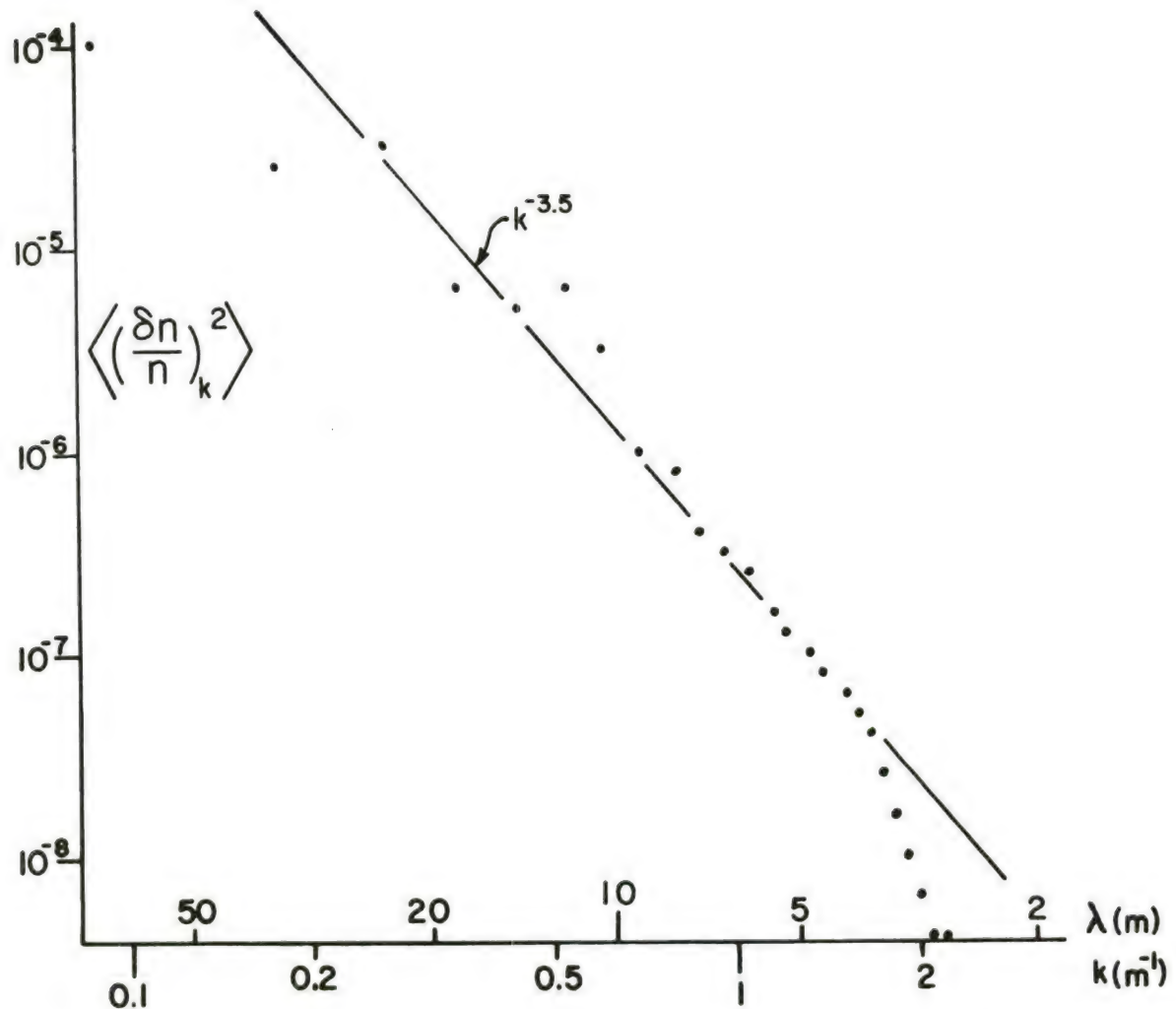


Fig. 6 — Type II electrojet power spectrum at $t = 2.7$ sec. This is the direction averaged power spectrum of the density fluctuations as depicted in Fig. 5. A power law of $k^{-3.5}$ fairly accurately describes the short wavelengths. The fall off below about 5 meters is due to grid size resolution capabilities in the present study.

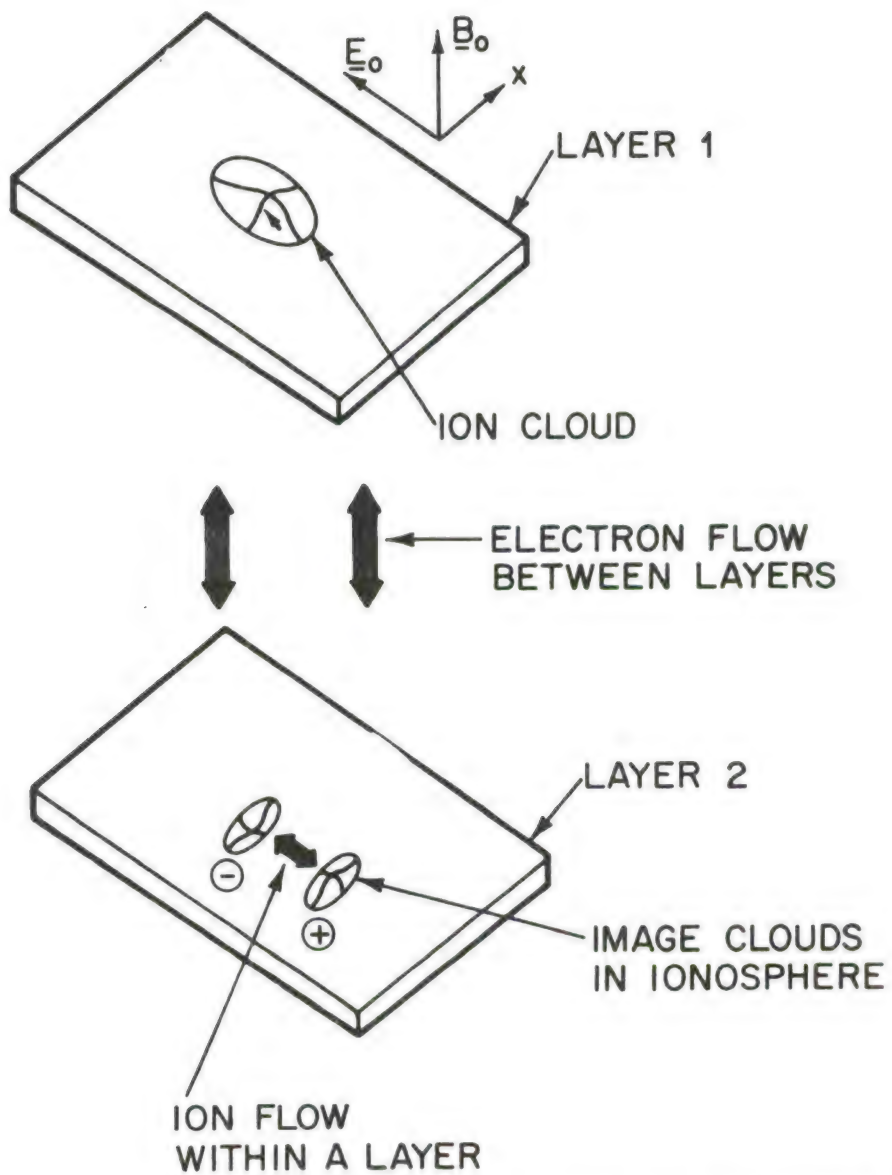


Fig. 7 — Two layered model for plasma cloud, images and striations. The earth's ambient magnetic field, B_0 , is in the z direction and taken constant. The ambient electric field, E_0 , is transverse to B_0 . The plasma cloud is in layer 1 and image clouds (positive and negative ion enhancements) in the background ionosphere are induced in layer 2. The model allows ion flow within each layer and electron flow between each layer along magnetic field lines. The model is two dimensional in the x - y plane. Each layer is described by its own parameters such as ion-neutral collision frequencies, Pedersen conductivities, etc., and these are taken to be constant within each layer. Typically layer 1 is in the F region at about 200-250 km and layer 2 is in the E region at about 150 km.

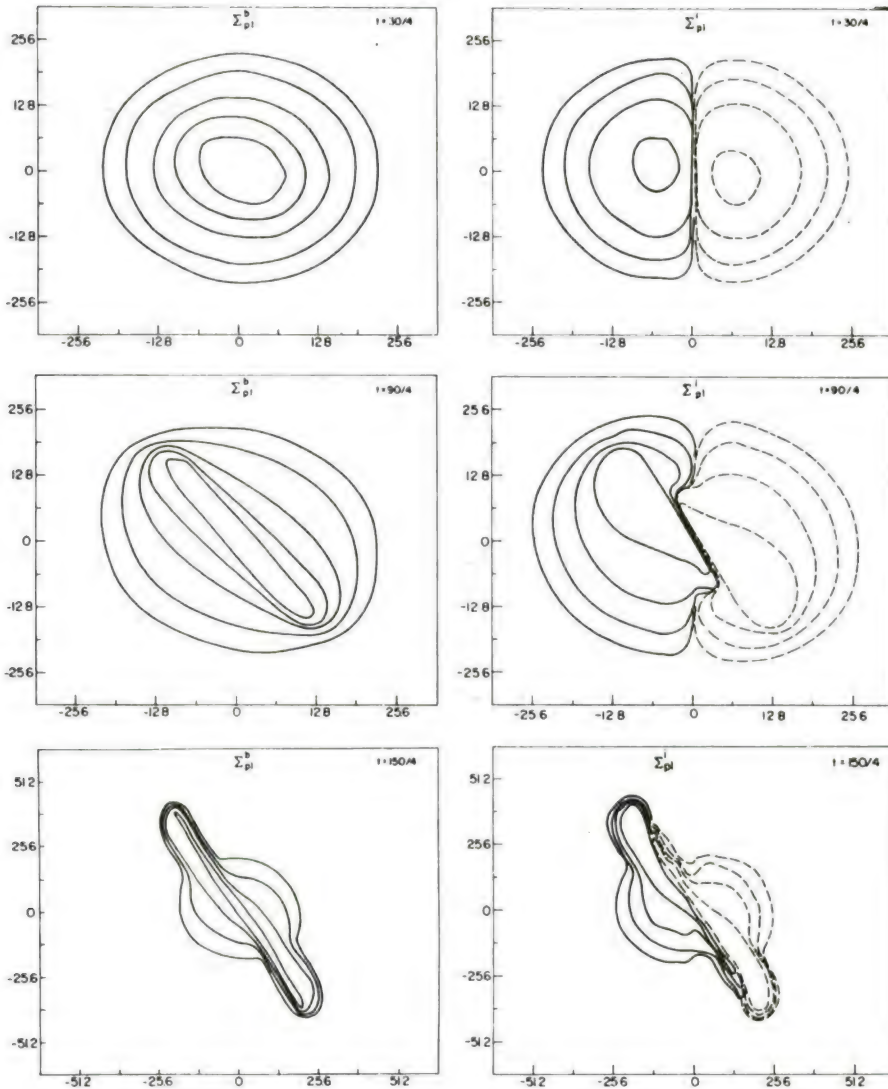


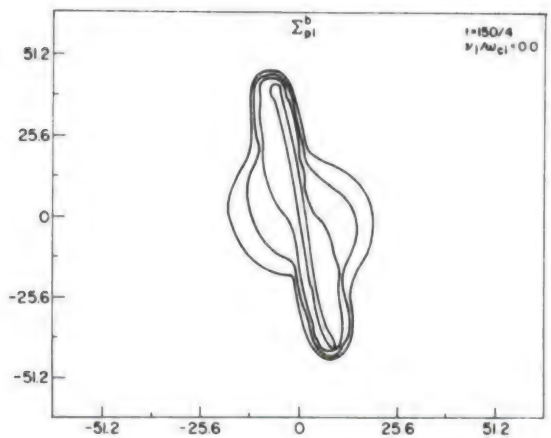
Fig. 8 — Nonlinear evolution of barium cloud Pedersen conductivity (Σ_{p1}^b) and ionospheric image Pedersen conductivity Σ_{p1}^i for a small cloud:

$$\Sigma_p^b / \Sigma_p^i \sim \epsilon$$

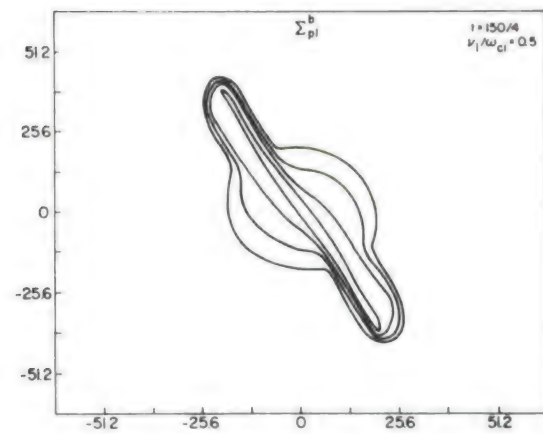
and

$$\Sigma_p^{i1} / \Sigma_p^{i0} = \epsilon^{1/2} \Sigma_{p1}^i, (\nu_i / \Omega_i) \cdot [1 + (\nu_i / \Omega_i)^2]^{-1} (\Sigma_p^b / \Sigma_p^{i0}) = \epsilon \Sigma_{p1}^b,$$

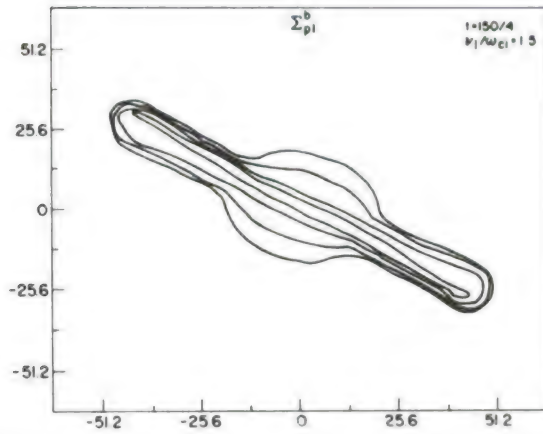
where Σ_p^{i0} is the zeroth order background ionospheric conductivity assumed to be constant. These solutions are with no diffusion, $T = 0$, $\nu_i / \Omega_i = 0.5$, the ambient electric field \underline{E}_0 in the x direction, \underline{B}_0 out of the paper so that the $\underline{E}_0 \times \underline{B}_0$ velocity frame is downward (the frame in which these results are depicted). A grid of 128×128 was employed, with $L = 8$ mesh spaces and periodic boundary conditions. The innermost contours for Σ_{p1}^b are the largest and for the images Σ_{p1}^i the innermost contours have the largest absolute values (solid lines depict positive enhancements and dashes negative enhancements, i.e., depletions, of background ionospheric ions). Note that the scales have been changes in the third row. Dimensionless time is given in the upper right.



(a)



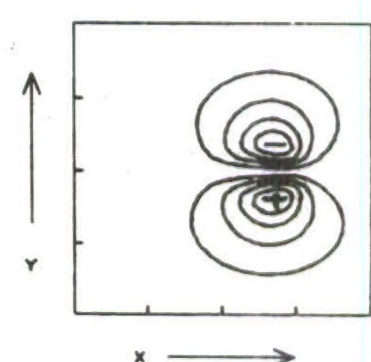
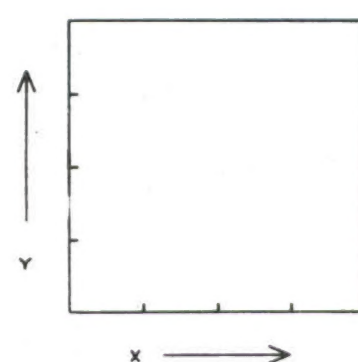
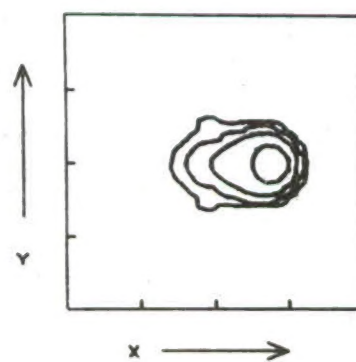
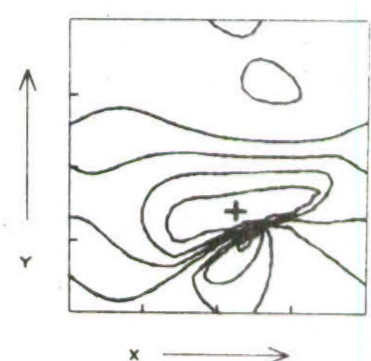
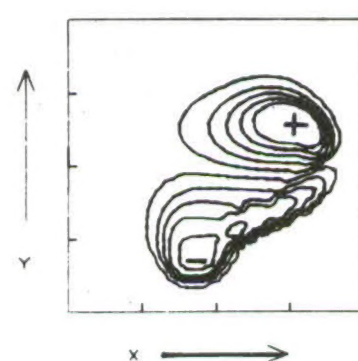
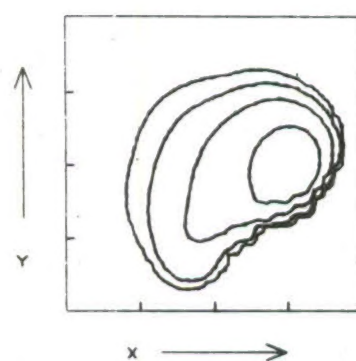
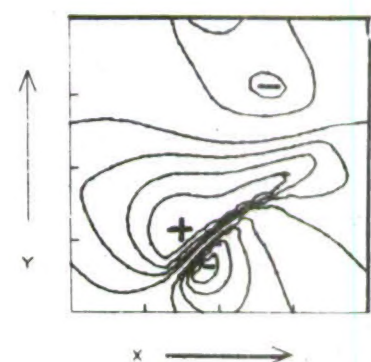
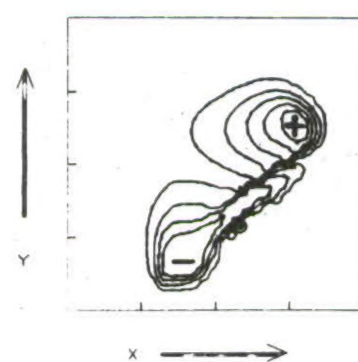
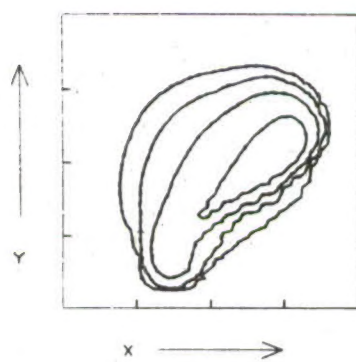
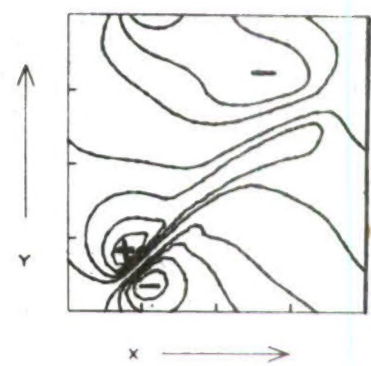
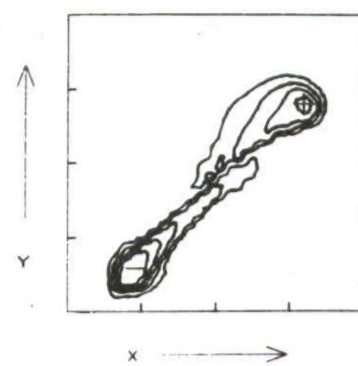
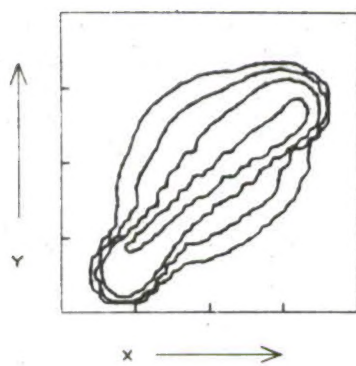
(b)



(c)

Fig. 9 — Late-time development of barium cloud Pedersen conductivities for different values of ν_i/Ω_i (0.0, 0.5 and 1.5). All other parameters are the same as in Fig. 8. As ν_i/Ω_i decreases the cloud lines up more with $\underline{E}_o \times \underline{B}_o$ direction (negative y), obeying the nonlinear prediction $\theta = \tan^{-1} (\nu_i/\Omega_i)$, where θ is the angle between the elongated axis of the cloud and $\underline{E}_o \times \underline{B}_o$ direction.

Fig. 10 — Nonlinear dynamical motion of large 2D barium clouds coupled to the background ionosphere. →
 This represents the late time behavior of the height-integrated Pedersen conductivities for the barium cloud and the induced ionospheric images (left and center columns, respectively) and the corresponding electrostatic potential Ψ (right column). From top to bottom the results are for $\Sigma_p^b/\Sigma_p^i = 0.1, 1.0, 4.0$ and ∞ (uncoupled case), i.e., $\Sigma_p^b/\Sigma_p^{i0} \propto \exp - [x^2 + y^2]/L^2$ at $t = 0$ and the ratios represent the peak barium conductivity to unperturbed background ionosphere conductivity, at times $t = 800$ (20), 250 (6.25), 150 (3.75) and 350 (8.75) sec, respectively, where the numbers in parentheses are time in units of LB/cE_0 . The collision frequency parameters are $\nu_i/\Omega_i = 0.5$ and $\nu_b/\Omega_b = 0.005$. In these cases $E_0 = 5$ mV/m and is in the negative y direction, $B_0 = 0.5$ gauss in the positive z direction and these figures are in the $E_0 \times B_0$ drift frame, which is in the negative x direction. L is 4 mesh spaces (4 km) and the mesh is 32×32 , so that each tick mark is 8 km. From the interior of the cloud the barium contours are $e^{-1}, e^{-3}, e^{-5}, e^{-7}$ times the maximum value of the unperturbed height integrated barium Pedersen conductivity, Σ_p^b . For the $\Sigma_p^b/\Sigma_p^i = 0.1$ case the ionospheric contours are at $1.0 \pm 0.1, \pm 0.2, \pm 0.3, \pm 0.4, \pm 0.5$ times Σ_p^i (proceeding inward), whereas, for the $\Sigma_p^b/\Sigma_p^i = 1.0$ and 4.0 cases these contours are $1.0 \pm 0.1, \pm 0.3, \pm 0.5 \pm 0.7, \pm 0.9$ times Σ_p^i . The regions of relative enhancement and depletion of the background ionospheric ions are marked with plus and minus signs, respectively. The sign of Ψ is indicated by plus and minus signs in regions of extrema. These cases are representative of F region barium (plasma) clouds coupled to a background E region ionosphere.



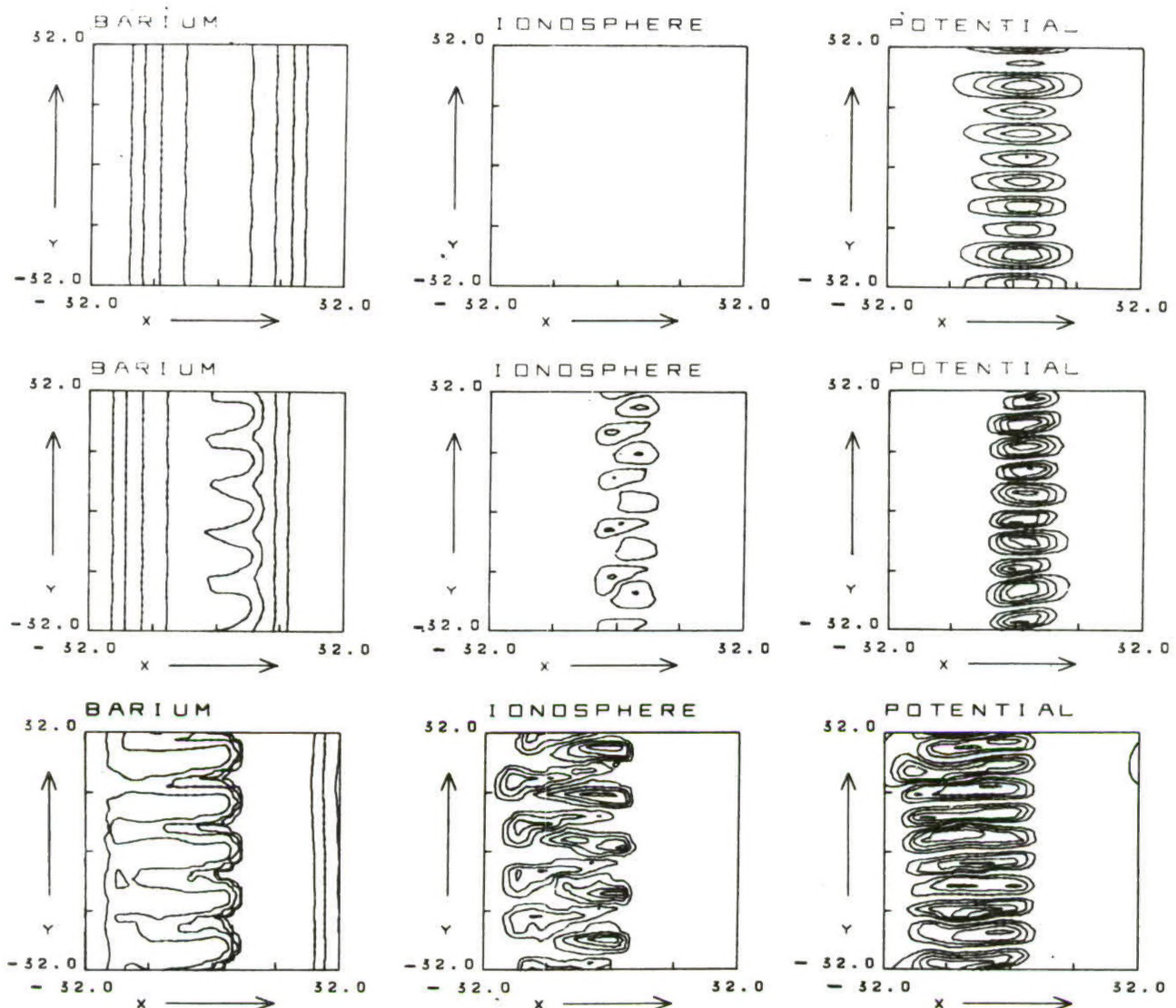


Fig. 11 — Time evolution of an initially 1D barium cloud with an initial perturbation (striations) coupled to the background ionosphere. The initial barium cloud Pedersen conductivity is given by $\Sigma_p^b/\Sigma_p^{i0} = \exp[-x^2/L^2] [1 + e^{-3} \sin(10\pi y/64)] + 0.01$ (i.e., $\Sigma_p^b/\Sigma_p^{i0} = 1.0$). The 0.01 term represents a background F region and is not to be confused with the background ionospheric E region (where imaging is occurring) depicted in the figures. The geometry and magnitude of E_o and B_o are the same as in Fig. 10, as is the format for the figures. In this case the collision frequency parameters are $\nu_i/\Omega_i = 0.1$ and $\nu_b/\Omega_b = 0.005$. The times depicted are $t = 49.5$ (0.62), 643.5 (8.04) and 1046 (13.08) sec, respectively. The numbers in parentheses are times in units of $L B_o/cE_o$. Here L is 8 mesh spaces (8 km) and the mesh is 64×64 . The barium contours are now e^{-1} , e^{-3} , e^{-5} , e^{-7} plus the background (0.01) times the maximum value of the height integrated Pedersen conductivity of the cloud. The image contours are the same as the 2D $\Sigma_p^b/\Sigma_p^{i0} = 1.0$ case. Note the striation growth on the backside (steepened side), i.e., side away from direction of $E_o \times B_o$ motion. Also at late time note the finger formation on this backside (nonlinear state).

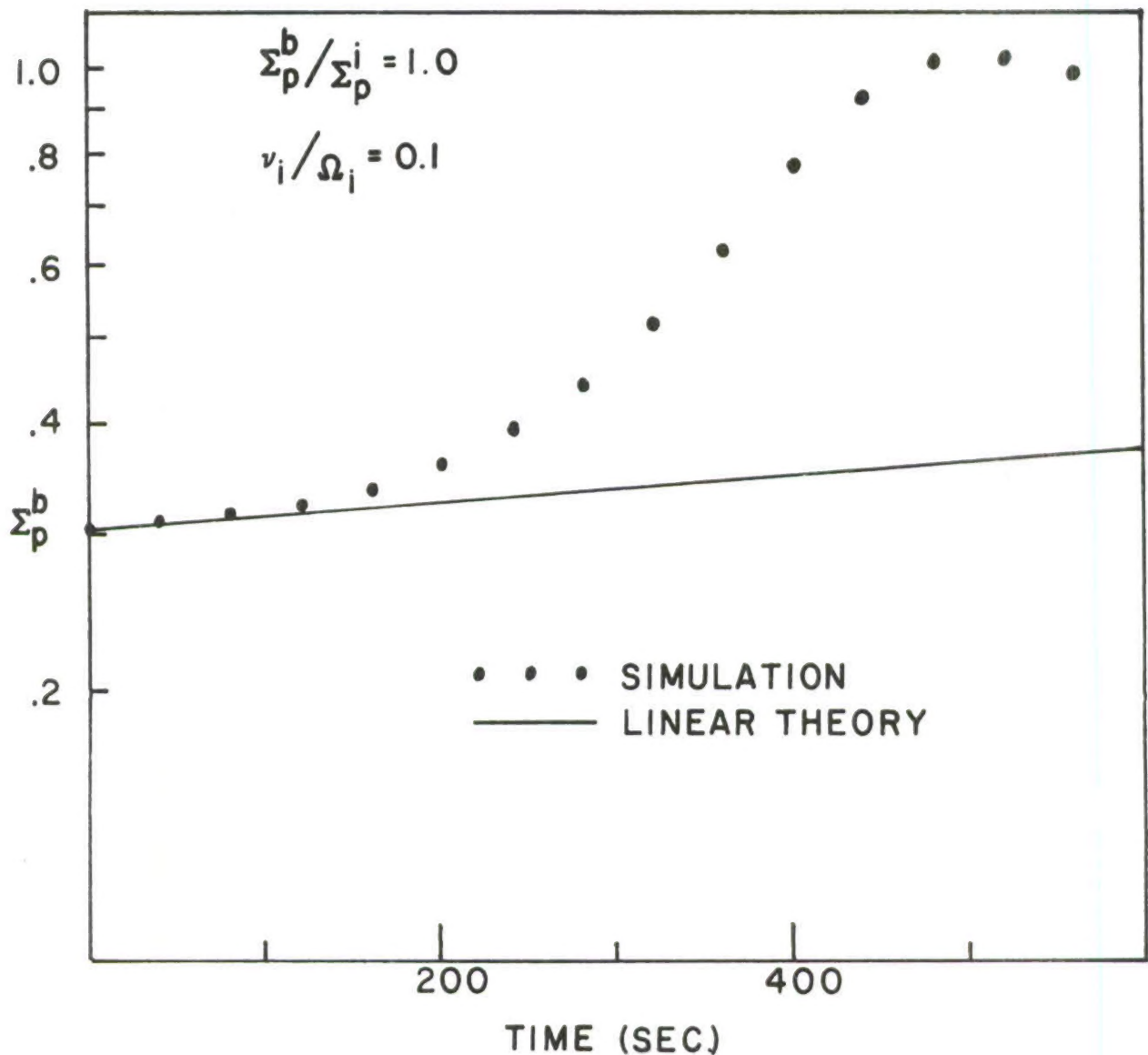


Fig. 12 — Pedersen conductivity in striation region of cloud versus time for 1D simulation depicted in Fig. 11. The dots indicate the values from the simulation and the solid line depicts the values predicted by linear theory, i.e., a linear perturbation analysis of the full set of Eqs. (13), (15), and (16). The agreement out to early times (~ 200 sec) is quite good and then the system takes on a nonlinear character.